Optics Communications 526 (2023) 128852

Contents lists available at ScienceDirect

Optics Communications

journal homepage: www.elsevier.com/locate/optcom

Tunable dual-frequency coherent Doppler lidar using bi-directional electro-optic modulation in a Sagnac loop

Lu Wang [a,b,1], Lijie Zhao [b,1], Yunpeng Zhang [b], Yunbin Wu [b], Haiyun Xia [b,c,d,*]

[a] Department of Electronic Information Engineering, Hefei University, Hefei, Anhui 230601, China
[b] School of Earth and Space Science, University of Science and Technology of China, Hefei, 230026, China
[c] Hefei National Laboratory for Physical Sciences at the Microscale, University of Science and Technology of China, Hefei, 230026, China
[d] CAS Center for Excellence in Comparative Planetology, University of Science and Technology of China, Hefei, 230026, China

ARTICLE INFO

Keywords:
Dual-frequency coherent Doppler lidar
Bi-directional electro-optic phase modulation
Envelope-demodulation

ABSTRACT

A novel tunable dual-frequency coherent Doppler lidar (DF-CDL) for velocity detection is proposed and experimentally demonstrated. In the laser source, although dual-frequency laser light can be generated by an electro-optic intensity modulator biased in the double-sideband suppressed-carrier mode, a slight drift in the direct-current (DC) bias voltage leads to a non-ideal carrier suppression. To address this problem, bi-directional electro-optic phase modulation in a Sagnac loop is employed. Due to the use of electro-optic phase modulators, no bias voltage is needed, resulting in no bias drifts. In the signal processing module, since the envelope of the Doppler signal is a cosine function of the differential Doppler shift, envelope-demodulation is employed to directly derive the differential Doppler shift from the analog Doppler signal. Due to the low-frequency characteristic of the differential Doppler shift, the sampling rate request of the ADC is reduced. In the experiments, the performance of the DF-CDL is validated under the conditions of different dual-frequency spacings and different target speeds. A speed measurement of 10.01 mm/s with a relative error of 0.10% is achieved when the dual-frequency spacing is 40 GHz and the target speed is 10 mm/s.

1. Introduction

Coherent Doppler lidar (CDL) is promising in scientific research and engineering applications [1–4], especially in velocity detection [5]. Unlike the use of single-frequency laser light in conventional single-frequency coherent Doppler lidar (SF-CDL), dual-frequency coherent Doppler lidar (DF-CDL) uses dual-frequency laser light with two optical frequency components spaced by a radio frequency (RF) [6].

SF-CDL derives the velocity of a moving target from the Doppler shift of the target backscattered signal [7]. In detail, the target backscatter signal is mixed with a local oscillator, resulting in a Doppler signal. The frequency of the Doppler signal is the Doppler shift. Nevertheless, coherent detection is highly phase-sensitive, and phase noise broadens the spectral width of the Doppler signal and decreases the carrier-to-noise ratio (CNR), thus limiting the resolution and accuracy of the Doppler measurement. The phase noise mainly includes the optical phase noise caused by the natural linewidth or frequency instability of the optical frequency and the speckle noise caused by target roughness or atmospheric turbulence.

For DF-CDL, velocity detections are based on differential Doppler shift measurement, thus improving the robustness to the phase noise [8]. The differential Doppler shift is the difference between the two Doppler shifts, and thus the phase noise of the differential Doppler signal is the difference between the phase noises of the two Doppler signals. Therefore, the optical phase noise can be reduced by locking the phases of the two optical frequency components. In other words, the optical phase noise is related to the linewidth and stability of the RF instead of the optical frequency. Moreover, the speckle noise, which is inversely proportional to wavelength, also be significantly reduced because the wavelength of the RF is much longer than that of the optical frequency. Applying this unique advantage, DF-CDL not only offers good performance in detecting target [9,10] and wind fields [11] but also provides better immunity to target roughness [8] and atmospheric turbulence [12,13].

The dual-frequency laser source is an important part of a DF-CDL system. On the one hand, a high-coherence dual-frequency laser source is needed to reduce the optical phase noise. The coherence includes the linewidth and stability of the dual-frequency spacing. In early works, two independent laser beams with a known frequency difference were overlapped to generate dual-frequency laser light, but it was difficult to lock the phases of these two beams [14]. Recently, this aim was realized

* Corresponding author at: School of Earth and Space Science, University of Science and Technology of China, Hefei, 230026, China.
E-mail address: hsia@ustc.edu.cn (H. Xia).
[1] Authors contribute equally to this work.

https://doi.org/10.1016/j.optcom.2022.128852
Received 18 April 2022; Received in revised form 28 July 2022; Accepted 1 August 2022
Available online 10 August 2022

by phase-locking two individual lasers to a Mach–Zehnder interferometer [15]. Besides, the high-coherence can be realized by a master laser optically injecting a slave semiconductor laser with an RF synthesizer which is used for phase-locking the two optical frequency components emitted by the SL [8,10]. On the other hand, to enable a dynamic trade-off between the sensitivity of the Doppler measurement and the robustness to the speckle noise, a tunable dual-frequency laser source is also needed. The tunability can be realized by a mode-locked laser with a wavelength selective switch (WSS). To improve the suppression of undesired modes, a Fabry–Perot filter (FPF) is needed before the WSS [16]. Compared to the use of two lasers or filters, the electro-optic modulator is an attractive alternative configuration. For example, the double-sideband signal generated by a Mach–Zehnder modulator (MZM) biased in the double-sideband suppressed-carrier mode can be used as dual-frequency laser light [17]. Benefiting from the modulation property, the phases of the two sidebands are highly coherent, and the spacing of the two sidebands can be easily tuned by changing the RF signal frequency. Nevertheless, a slight drift in the direct-current (DC) bias voltage results in a residual carrier. In this work, to address the bias drifts, bi-directional electro-optic phase modulation in a Sagnac loop is employed to suppress the carrier with no need of the bias voltage.

Furthermore, in the signal processing module of a DF-CDL system, the analog Doppler signal is firstly digitalized by a high-speed analog-to-digital converter (ADC) and then used for deriving the differential Doppler shift [16]. In this work, as an alternative method, envelope-demodulation is employed to directly derive the differential Doppler signal from the analog Doppler signal. Therefore, there is no need to digitize the Doppler signal. Due to the differential Doppler shift in Hz magnitude, the digitization of the differential Doppler signal is easier than that of the Doppler signal. This is expected to reduce the sampling rate request of the ADC.

The rest of this paper is organized as follows: Section 2 illustrates the proposed DF-CDL system layout along with the signal spectra at different steps. Section 3 presents the velocity detection experiments. The tunability of the dual-frequency laser source is tested, and the measurement sensitivity and error are analyzed. The conclusion is given in Section 4.

2. Principle and experimental setup

The schematic of the DF-CDL is shown in Fig. 1. The key parameters of the DF-CDL is listed in Table 1. A seed laser provides a continuous optical carrier with a power of 20 mW. After going through an isolator, the carrier enters a Sagnac loop via a 3 dB polarization-maintaining (PM) coupler. The Sagnac loop is comprised of the coupler and two PM electro-optic phase modulators (EOM_1 and EOM_2, MPZ-LN-20, iXblue). A closed-loop temperature controller is adopted, which ensures temperature stability within ±0.001°C [18]. The PM components and temperature controller is used for ensuring the loop's stability [19]. The fiber length of the loop is about 4 m. To suppress the carrier, EOM_1 is placed on the clockwise (CW) path of the loop away from the loop center and EOM_2 is placed on the counter-clockwise (CCW) path at the loop center. On the one hand, the carrier in the CW path is modulated by EOM_1 in the forward direction and by EOM_2 in the backward direction. On the other hand, the carrier in the CCW path is modulated by EOM_2 in the forward direction and by EOM_1 in the backward direction. The two EOMs are fed by the RF signals with the same frequencies and powers of 10 mW. In traveling wave EOM, when carrier and RF signal travel in opposite directions, the modulation index is small due to the velocity mismatch effect [20]. Therefore, the carrier in the CW path is mainly modulated by EOM_1 and in the CCW path is mainly by EOM_2. Since there is 90° optical phase shift when laser light travels through the coupler, the modulated signals in the CW and the CCW paths at the loop output are 180° out of phase [19]. Therefore, the carrier can be largely suppressed at the loop output.

The optical spectrum at the loop input is shown in Fig. 1(a). It is an optical carrier of single-frequency laser light. The electric field can be described as $E_{in}\exp\left(j\omega_c t\right)$, where E_{in} and $\omega_c = 2\pi\upsilon_c$ are the amplitude and angular frequency, respectively. The carrier is split into two equal portions entering the loop in CW and CCW paths. The electric field of the modulated signal in the CW path at the loop output is given by [21]:

Table 1
Key parameters of the DF-CDL.

	Parameter	Value
Laser	Wavelength (nm)	1548.5
	Linewidth (kHz)	3
EOM	Electro-optic bandwidth (GHz)	0–20
AOM	Frequency shift (MHz)	80
Collimator	Diameter (mm)	2
BD	Bandwidth (MHz)	200

$$E_{CW} = \frac{1}{2} l E_{in} \exp\left\{j[\omega_c t + \beta\cos(\omega_m t + \phi)]\right\}. \tag{1}$$

where l is the modulator optical insertion loss, β is the modulation index, $\omega_m = 2\pi f_m$ is the RF signal angular frequency, and $\phi = \omega_m n\Delta L/c$ is the phase difference between the modulated signals in CW and CCW paths, with n being the fiber refractive index, ΔL being the distance of EOM_1 away from the loop center, c being the light speed in a vacuum. Similarly, the electric field of the modulated signal in the CCW path at the loop output is given by:

$$E_{CCW} = -\frac{1}{2} l E_{in} \exp\left\{j[\omega_c t + \beta\cos(\omega_m t)]\right\}, \tag{2}$$

The total electric field at the loop output is the summation of E_{CW} and E_{CCW}, which can be written as:

$$E_{out} = \frac{1}{2} l E_{in} \exp(j\omega_c t)\left\{\exp[\beta\cos(\omega_m t + \phi)] - \exp[\beta\cos(\omega_m t)]\right\}, \tag{3}$$

After decomposing E_{out} into a Fourier series using Jacobi–Anger identity in small signal conditions, it can be expressed as [22]:

$$E_{out} = \frac{1}{2}\beta l E_{in}\exp(j\omega_c t + \frac{\pi}{2})\left[\cos(\omega_m t + \phi) - \cos(\omega_m t)\right], \tag{4}$$

The optical spectrum at the loop output is shown in Fig. 1(b). It is the dual-frequency laser light generated by double-sideband suppressed-carrier modulation. Benefiting from the bi-directional modulation in the loop and the 180° phase difference between the modulated signals at the loop output, the carrier is largely suppressed. The optical frequencies of the two sidebands are $\upsilon_1 = \upsilon_c - f_m$ and $\upsilon_2 = \upsilon_c + f_m$. The spacing of the two sidebands is $\Delta\upsilon = 2f_m$. It highlights that the dual-frequency spacing is double the RF signal frequency, thus broadening the tunable range of the spacing. Since the carrier power is largely suppressed by the Sagnac loop and the sideband power is small, the power of the dual-frequency laser light at the loop output is only 200 nW.

To detect target velocity, the dual-frequency laser light is amplified to 0.1 mW. Then, it is split into transmitted light and reference light via a 99:1 PM splitter. The transmitted light is converted into spatial light by a collimator and transmitted to a retroreflector moving away from the collimator. The retroreflector is placed about 1 m away from the collimator and mounted on a nanometer linear positioning stage (NLPS) which is driven by a servo-controlled Piezoelectric transducer (PZT). To distinguish the direction of retroreflector movement, the reference light is frequency-shifted by an acousto-optic modulator (AOM). The power of the retroreflector backscatter signal coupled to the collimator is 30 μW. As shown in Fig. 1(c), there are two Doppler shifts f_{d1} and f_{d2} at the two optical frequency components υ_1 and υ_2 of the backscatter signal, respectively. Since the retroreflector moves away from the DF-CDL, the two Doppler shifts are positive. The backscatter signal is then mixed with the reference light via a 3 dB PM coupler and detected on a balanced detector (BD). Since the BD's bandwidth is sufficiently narrow, only two Doppler shifts can pass through, resulting in a Doppler signal as shown in Fig. 1(d). Fig. 1(e) shows a differential

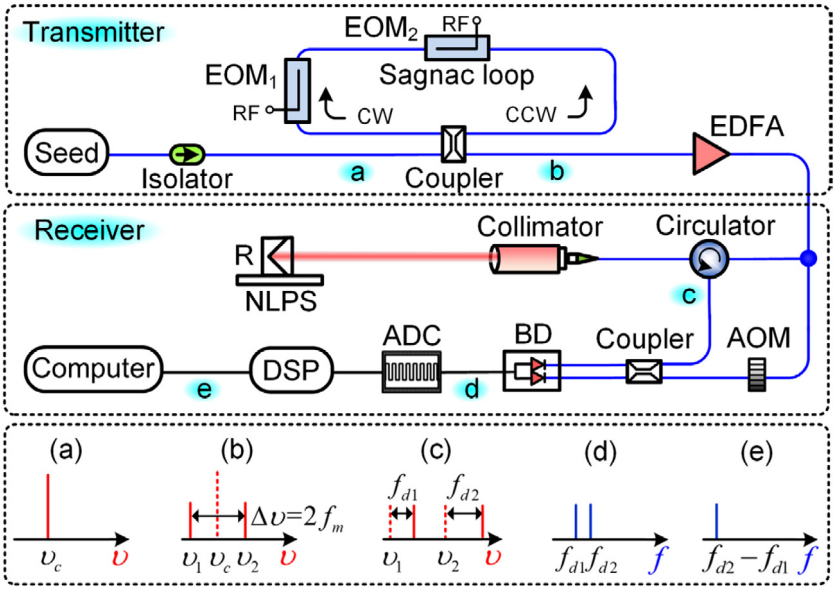

Fig. 1. Schematic of the DF-CDL (in the upper and middle dashed line boxes) and the signal spectra at different steps (in the lower dashed line box) [labeled as (a)–(e)]. EOM, electro-optic modulator; RF, radio-frequency signal; EDFA, erbium-doped fiber amplifier; R, Retroreflector; NLPS, Nanometer linear position stage; AOM, acousto-optic modulator; BD, balanced detector; ADC, analog-to-digital converter; DSP, digital signal processor. (a) Single-frequency laser light at the Sagnac loop input. (b) Dual-frequency laser light at the loop output. (c) Target backscatter signal. (d) Doppler signal. (e) Differential Doppler signal.

Doppler signal extracted from the Doppler signal. The frequency of the differential Doppler signal is the differential Doppler shift. Considering the Doppler shift $f_d = 2sv_c/c$ is proportional to the target speed s, the differential Doppler shift also contains the target speed information. It can be expressed as [6]:

$$f_{d2} - f_{d1} = \frac{2s\Delta v}{c}, \tag{5}$$

where s is the target speed, Δv is the dual-frequency spacing, c is the light speed in a vacuum. Since all other parameters are known, it is able to get the target speed by measuring the differential Doppler shift.

3. Experimental results

In the experiments, to test the tunability of the dual-frequency laser source, an RF signal generator is used for providing different RF signals. Fig. 2 shows the optical spectra of the dual-frequency laser light obtained from the loop output. The black line denotes the optical carrier of single-frequency laser light. The pink dash-dotted line, the green dashed line, and the blue dotted line denote the dual-frequency laser light with different dual-frequency spacings. The power difference between the carrier location and the sideband location of the dual-frequency laser light is about 30dBm. It indicates the success of the carrier suppression. The positions of the two sidebands are symmetrically located about the carrier and shifted away from the center along with the increased RF signal frequency. The dual-frequency spacing of 20, 30, or 40 GHz is tuned when the RF signal frequency is set to 10, 15, or 20 GHz, respectively. It is confirmed that the dual-frequency spacing can be easily tuned by changing the RF signal frequency.

Under the condition of a dual-frequency spacing of 40 GHz and a target speed of 10 mm/s, the normalized temporal waveform of the Doppler signal and its enlargement are shown in Fig. 3(a) and (c), respectively. The corresponding normalized power spectrum and its enlargement are shown in Fig. 3(b) and (d), respectively. By subtracting the AOM frequency, the Doppler shifts of about 12.91 kHz are observed. To derive the differential Doppler shift from the Doppler signal, one method is to firstly digitalize the analog Doppler signal by an ADC and then calculate the square of the digital Doppler signal by a digital signal processor (DSP). Among the resulting four terms, the differential Doppler shift is the lowest frequency, and thus it can be obtained by

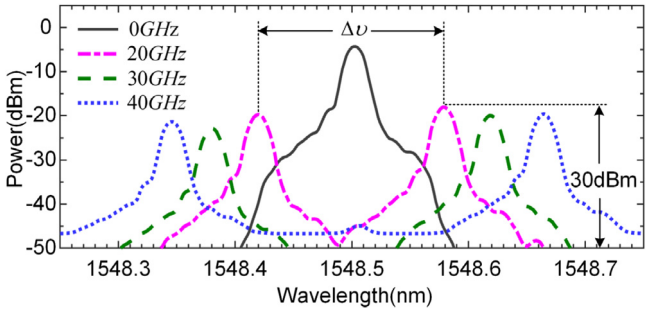

Fig. 2. Optical spectra of the dual-frequency laser light at the Sagnac loop output with different dual-frequency spacings.

a low-frequency filter [16]. Here, as an alternative method, envelope-demodulation is employed. Since there are two Doppler shifts, the Doppler signal is the superposition of the two cosine waves with similar amplitudes and frequencies. The amplitude of the composite wave should be modulated by the frequency difference between the two cosine waves. In other words, the envelope of the Doppler signal is a cosine function of the differential Doppler shift. Therefore, it should be possible to directly derive the differential Doppler shift from the analog Doppler signal by utilizing the envelope-demodulation.

In detail, a root-mean-square (RMS) envelope-demodulation with a sampling rate of 300 Hz is utilized to demodulate the envelope of the Doppler signal in Fig. 3(a). The RMS calculation is used for mitigating the envelope fluctuations in Fig. 3(c). Fig. 3(e) and (f) show the demodulated results, including the normalized waveform and power spectrum of the upper envelope. The frequency peak of the power spectrum equals the differential Doppler shift. The spectral width is related to the RF linewidth instead of the laser linewidth or other optical noise. The sampling time of the waveform for FFT calculation is 2 s, corresponding to a frequency resolution of 0.5 Hz. The sampling time depends on the target speed. If the target speed is 0.1 m/s, the sampling time of 0.2 s will be enough because a larger target speed corresponds to a larger differential Doppler shift, leading to a high tolerance of frequency resolution. The number of the points for FFT calculation is 100 times the sampling rate, corresponding to a frequency

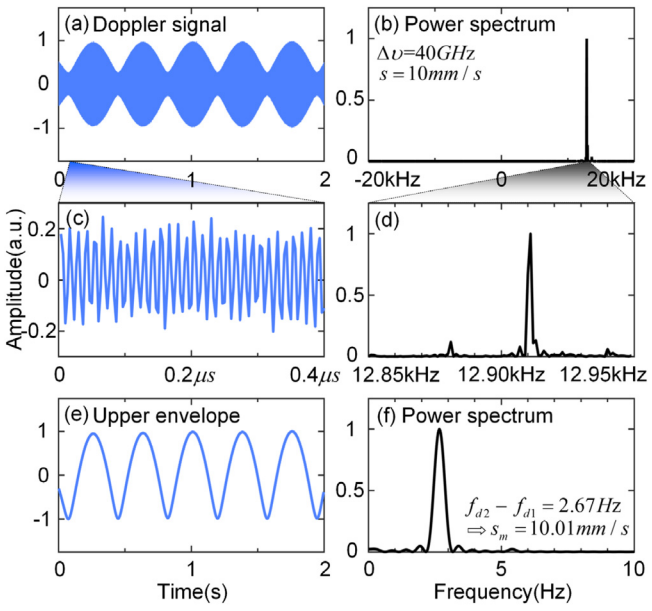

Fig. 3. (a) Normalized temporal waveform of the Doppler signal and (c) its enlargement. (b) Normalized power spectrum of the Doppler signal and (d) its enlargement. (e) Normalized waveform and (f) power spectrum of the upper envelope of Doppler signal.

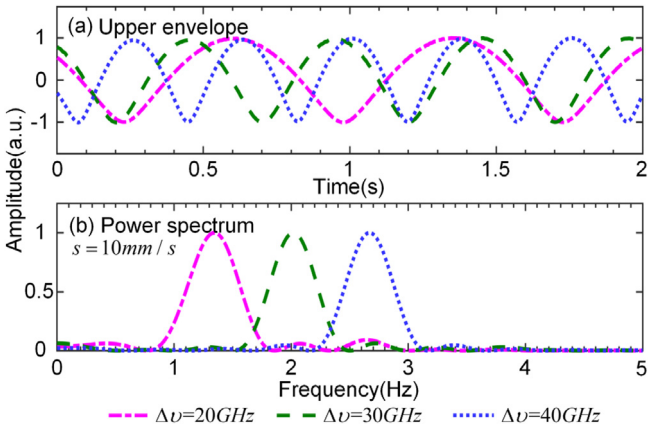

Fig. 4. (a) Normalized waveforms and (b) power spectra of the upper envelopes with different dual-frequency spacings and a fixed target speed of 10 mm/s.

interval of 0.01 Hz. As shown in Fig. 3(f), the measured differential Doppler shift is 2.67 Hz. According to Eq. (4), a speed measurement of 10.01 mm/s is calculated, achieving a relative error of 0.10%.

Under the conditions of different dual-frequency spacings and a fixed target speed of 10 mm/s, the normalized waveforms and power spectra of the upper envelopes are shown in Fig. 4(a) and (b), respectively. As the dual-frequency spacing increases, the period of the upper envelope waveform shortens. The differential Doppler shift increases from 1.33 to 2.67 Hz as the dual-frequency spacing increases from 20 to 40 GHz. The results indicate that when the dual-frequency spacing increases, the differential Doppler shift increases, as same as the measurable minimum speed decreases, and thus the measurement sensitivity is improved. But meanwhile, when the dual-frequency spacing increases, as same as the wavelength of the RF signal shortens, the speckle noise increases [8], and thus the measurement robustness is weakened. Therefore, a trade-off between the measurement sensitivity and robustness can be enabled by the tunability of dual-frequency laser source.

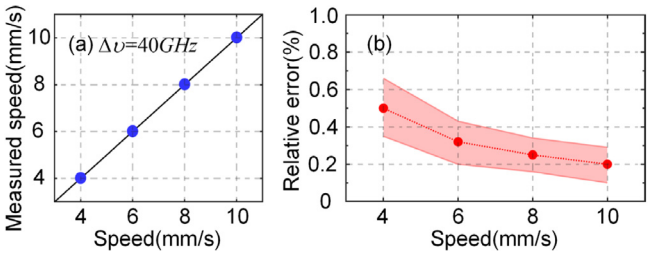

Fig. 5. (a) Average speed measurements and (b) their relative errors with a fixed dual-frequency spacing of 40 GHz and different target speeds.

Fig. 5(a) and (b) show the average speed measurements and their relative errors under the conditions of a fixed dual-frequency spacing of 40 GHz and different target speeds. In Fig. 5(a), the blue dots denote the average speed measurements when the target speeds are preset to 4, 6, 8, and 10 mm/s. The black line denotes y=x, showing a good agreement between the average speed measurements and the preset target speeds. In Fig. 5(b), the red shaded areas denote the relative error ranges of the speed measurements in Fig. 5(a). The average relative errors denoted by the red dots achieve a value below 0.50%, verifying the capability of the DF-CDL.

4. Discussion

In this paper, to show the envelope-demodulation process, the demodulation is achieved by digital signal processing. A high-speed ADC is still used for digitalizing the analog Doppler signal. The digital Doppler signal is used for visually showing the process of demodulating the sinusoidal envelope. In fact, instead of digital signal processing, the analog Doppler signal could be directly demodulated by an electronic envelope detector to obtain the envelope. The envelope is then digitalized to measure the differential Doppler shift. Due to the differential Doppler shift in Hz magnitude, a low-speed ADC with a sampling rate of Hz magnitude is enough. Furthermore, since the DF-CDL can offer simultaneous velocity and range measurements [17] and provide better immunity to atmospheric turbulence [12], it could be a preferable choice in remote sensing.

5. Conclusions

A tunable DF-CDL is demonstrated based on the bi-directional electro-optic phase modulation in a Sagnac loop, realizing the double-sideband suppressed-carrier modulation with no bias drifts. The new scheme offers flexible tuning of the dual-frequency spacing by changing the RF signal frequency, thus allowing for a dynamic trade-off between the sensitivity and robustness of the Doppler measurement. The velocity detection experiments are carried out under the conditions of the dual-frequency spacings of 20, 30, and 40 GHz and the target speeds of 4, 6, 8, and 10 mm/s, validating the performance of the DF-CDL. Furthermore, in the signal processing module, by utilizing the envelope-demodulation, velocity detection could be realized with a low sampling rate request of the ADC.

Funding

This work received no external funding.

Declaration of competing interest

The authors declare that they have no known competing financial interests or personal relationships that could have appeared to influence the work reported in this paper.

Data availability

Data will be made available on request.

References

[1] J.L. Yuan, H.Y. Xia, T.W. Wei, L. Wang, B. Yue, Y.B. Wu, Identifying cloud, precipitation, windshear, and turbulence by deep analysis of the power spectrum of coherent Doppler wind lidar, Opt. Express 28 (2020) 37406–37418, http://dx.doi.org/10.1364/OE.412809.

[2] T.W. Wei, H.Y. Xia, J.J. Hu, C. Wang, M.J. Shangguan, L. Wang, M.J. Jia, X.K. Dou, Simultaneous wind and rainfall detection by power spectrum analysis using a VAD scanning coherent Doppler lidar, Opt. Express 27 (2019) 31235–31245, http://dx.doi.org/10.1364/OE.27.031235.

[3] L. Wang, W. Qiang, H.Y. Xia, T.W. Wei, J.L. Yuan, P. Jiang, Robust solution for boundary layer height detections with coherent Doppler wind lidar, Adv. Atmos. Sci. 38 (2021) 1920–1928, http://dx.doi.org/10.1007/s00376-021-1068-0.

[4] L. Wang, J. Yuan, H. Xia, L. Zhao, Y. Wu, Marine mixed layer height detection using ship-borne coherent Doppler wind lidar based on constant turbulence threshold, Remote Sens. 14 (2022) 745, http://dx.doi.org/10.3390/rs14030745.

[5] Y. Zhang, Y. Wu, H. Xia, Spatial resolution enhancement of coherent Doppler wind lidar using differential correlation pair technique, Opt. Lett. 46 (2021) 5550–5553, http://dx.doi.org/10.1364/OL.442121.

[6] L. Morvan, N.D. Lai, D. Dolfi, J.-P. Huignard, M. Brunel, F. Bretenaker, A. Le Floch, Building blocks for a two-frequency laser lidar-radar: a preliminary study, Appl. Opt. 41 (2002) 5702–5712, http://dx.doi.org/10.1364/AO.41.005702.

[7] C. Wang, H.Y. Xia, M.J. Shangguan, Y.B. Wu, L. Wang, L.J. Zhao, J.W. Qiu, R.J. Zhang, 1.5μm Polarization coherent lidar incorporating time-division multiplexing, Opt. Express 25 (2017) 20663–20674, http://dx.doi.org/10.1364/OE.25.020663.

[8] C.-H. Cheng, C.-W. Lee, T.-W. Lin, F.-Y. Lin, Dual-frequency laser Doppler velocimeter for speckle noise reduction and coherence enhancement, Opt. Express 20 (2012) 20255–20265, http://dx.doi.org/10.1364/OE.20.020255.

[9] Y. Li, Y. Xing, Y. Gao, H. Zhang, Z. Zhang, C. Zhao, A dual-frequency continuous wave doppler lidar for velocity measurement at far distance, Microw. Opt. Technol. Lett. 63 (2021) 1–7, http://dx.doi.org/10.1002/mop.32797.

[10] R. Diaz, S.-C. Chan, J.-M. Liu, Lidar detection using a dual-frequency source, Opt. Lett. 31 (2006) 3600–3602, http://dx.doi.org/10.1364/OL.31.003600.

[11] J. Li, H. Xu, Performance analysis of dual-frequency lidar in the detection of complex wind field, Opt. Express 29 (2021) 23524–23539, http://dx.doi.org/10.1364/OE.431069.

[12] Z. Zheng, C. Zhao, H. Zhang, S. Yang, D. Zhang, H. Yang, J. Liu, Phase noise reduction by using dual-frequency laser in coherent detection, Opt. Laser Technol. 80 (2016) 169–175, http://dx.doi.org/10.1016/j.optlastec.2016.01.005.

[13] S. Wang, S.-H. Yang, X. Wu, C.-M. Zhao, Q.-H. Zhu, Experimental study on influence of atmospheric turbulence on coherence of dual-frequency laser, Chin. Phys. Lett. 27 (2010) 084202, http://dx.doi.org/10.1088/0256-307X/27/8/084202.

[14] W.L. Eberhard, R.M. Schotland, Dual-frequency Doppler-lidar method of wind measurement, Appl. Opt. 19 (1980) 2967–2976, http://dx.doi.org/10.1364/AO.19.002967.

[15] Y. Feng, W. Xie, Y. Meng, L. Zhang, Y. Dong, Dual-frequency Doppler velocimeter based on delay interferometric optical phase-locking, Opt. Lett. 46 (2021) 2103–2106, http://dx.doi.org/10.1364/OL.420402.

[16] V. Vercesi, D. Onori, F. Laghezza, F. Scotti, A. Bogoni, M. Scaffardi, Frequency-agile dual-frequency lidar for integrated coherent radar-lidar architectures, Opt. Lett. 40 (2015) 1358–1361, http://dx.doi.org/10.1364/OL.40.001358.

[17] D. Onori, F. Scotti, M. Scaffardi, A. Bogoni, F. Laghezza, Coherent interferometric dual frequency laser radar for precise range/Doppler measurement, J. Lightwave Technol. 34 (2016) 4828–4834, http://dx.doi.org/10.1109/jlt.2016.2589538.

[18] M. Shangguan, H. Xia, C. Wang, J. Qiu, G. Shentu, Q. Zhang, X. Dou, J.W. Pan, All-fiber upconversion high spectral resolution wind lidar using a Fabry–Perot interferometer, Opt. Express 24 (19322) (2016) http://dx.doi.org/10.1364/OE.24.019322.

[19] E.H.W. Chan, R.A. Minasian, Microwave photonic downconversion using phase modulators in a sagnac loop interferometer, IEEE J. Sel. Top. Quant. 19 (2013) 211–218, http://dx.doi.org/10.1109/JSTQE.2013.2263119.

[20] W.R. Leeb, A.L. Scholtz, E. Bonek, Measurement of velocity mismatch in traveling-wave electrooptic modulators, IEEE J. Quantum Electron. QE-18 (1982) 14–16, http://dx.doi.org/10.1109/JQE.1982.1071379.

[21] W. Li, J. Yao, Dynamic range improvement of a microwave photonic link based on bi-directional use of a polarization modulator in a Sagnac loop, Opt. Express 21 (2013) 15692–15697, http://dx.doi.org/10.1364/OE.21.015692.

[22] H. Emami, M. Hajihashemi, S.E. Alavi, S.M. Supaat, L. Bui, Microwave photonics instantaneous frequency measurement receiver based on a Sagnac loop, Opt. Lett. 43 (2018) 2233–2236, http://dx.doi.org/10.1364/OL.43.002233.